



Multiplexed ion beam imaging (MIBI) for characterization of the tumor microenvironment across tumor types

Jason Ptacek¹ · Darren Locke² · Rachel Finck¹ · Mary-Ellen Cvijic² · Zhuyin Li² · Jay G. Tarolli¹ · Murat Aksoy¹ · Yari Sigal¹ · Yi Zhang¹ · Matt Newgren¹ · Jessica Finn¹

Received: 17 December 2019 / Revised: 5 March 2020 / Accepted: 6 March 2020 / Published online: 23 March 2020
© The Author(s), under exclusive licence to United States and Canadian Academy of Pathology 2020

Abstract

An ability to characterize the cellular composition and spatial organization of the tumor microenvironment (TME) using multiplexed IHC has been limited by the techniques available. Here we show the applicability of multiplexed ion beam imaging (MIBI) for cell phenotype identification and analysis of spatial relationships across numerous tumor types. Formalin-fixed paraffin-embedded (FFPE) samples from tumor biopsies were simultaneously stained with a panel of 15 antibodies, each labeled with a specific metal isotope. Multi-step processing produced images of the TME that were further segmented into single cells. Frequencies of different cell subsets and the distributions of nearest neighbor distances between them were calculated using this data. A total of 50 tumor specimens from 15 tumor types were characterized for their immune profile and spatial organization. Most samples showed infiltrating cytotoxic T cells and macrophages present amongst tumor cells. Spatial analysis of the TME in two ovarian serous carcinoma images highlighted differences in the degree of mixing between tumor and immune cells across samples. Identification of admixed PD-L1+ macrophages and PD-1+ T cells in an urothelial carcinoma sample allowed for the detailed observations of immune cell subset spatial arrangement. These results illustrate the high-parameter capability of MIBI at a sensitivity and resolution uniquely suited to understanding the complex tumor immune landscape including the spatial relationships of immune and tumor cells and expression of immunoregulatory proteins.

Introduction

The diversity of cell types within the tumor microenvironment (TME) has become widely appreciated in the past decade. In addition to neoplastic cells, fibroblasts, vascular endothelial cells, and multiple immune cell subsets can often be found within the TME. The presence of specific T cell populations within the TME has been associated with patient survival in colorectal cancer (CRC) [1, 2]. This has been further developed into an Immunoscore to aid in staging CRC and its utility is being explored in melanoma and

breast cancer, among others [3, 4]. Other cell types, such as macrophages, have been shown to negatively affect anti-tumor immune responses in head and neck squamous cell carcinoma [5]. The recent successes of checkpoint blockade (anti-CTLA-4, anti-PD-1, and anti-PD-L1) targeting immune suppression within the TME have reshaped the care of patients with specific cancers. Despite these successes, more than half fail to have a durable response to treatment [6]. The cell types of the TME, their relations to each other, and their expression, or lack thereof, of specific checkpoint proteins may underlie the response to checkpoint blockade. Companion diagnostic tests have been developed but their accuracy indicates that there is biology that is yet understood. Multiplexing technology that both provides a census of the cell types present and their spatial relationships has been lacking because of an inability to distinguish a range of biomarkers at single cell resolution.

Fluorescent microscopy and laser scanning cytometry uses fluorophore-labeled probes to image tissue stained with around 6–8 markers [7, 8]. To image even greater numbers of targets, multiplex immunohistochemistry (mIHC) is

Supplementary information The online version of this article (<https://doi.org/10.1038/s41374-020-0417-4>) contains supplementary material, which is available to authorized users.

✉ Jason Ptacek
jptacek@ionpath.com

¹ Ionpath Inc, Menlo Park, CA, USA

² Bristol-Myers Squibb, Princeton, NJ, USA

performed using cyclical rounds of staining, imaging, and stripping a single formalin-fixed paraffin-embedded (FFPE) tissue section. Each round typically utilizes heat-induced antigen retrieval and alcohol dehydration that can degrade the tissue and the antigens present in an FFPE section. The cyclical nature leads to long processing times and challenges with image coregistration. Recent advances using CODEX (CO-Detection by indEXing) enables the tissue to be labeled in a single staining with a large panel of antibodies with each having a specific DNA-barcode and then imaged in a cyclical process. This has recently been performed to characterize the immune infiltrates in normal and lupus (MRL/lpr) murine spleens [9]. Multiplexing has also been achieved through the use of metal-labeled antibodies that are simultaneously detected with an imaging mass cytometer. This instrument uses an atmospheric laser ablation chamber interfaced to a mass cytometer [10, 11]. Despite these advances, these platforms have challenges with sample preparation, sensitivity, image resolution, or throughput limiting their wider adoption.

A recent addition to the field is multiplexed ion beam imaging (MIBI) with simultaneous detection of 40+ markers at subcellular resolution, enabling single cell segmentation, cell type classification defined by markers with a wide range of expression levels, and spatial analysis of the cells present in the TME [12–14]. MIBI is performed by staining tissue with a panel of metal-labeled antibodies and then imaging the tissue using time-of-flight secondary ion mass spectrometry. The masses of detected species are then assigned to target biomolecules given the unique metal isotope label of each antibody, creating multiplex images.

In the present study we sought to evaluate the applicability of MIBI across 15 tumor types. The staining panel was developed to define immune components and their spatial organization within the TME. Both high- and low-abundant markers were identified at subcellular resolution. Specific immune cell subsets including T cells, macrophages, and NK cells were identified using a gating strategy that leveraged the high dimensionality of the data. With this information it was possible to identify which of these cell populations expressed the immune checkpoint markers PD-1 and PD-L1 in addition to quantifying the distances between the PD-1 and PD-L1 positive cells.

Materials and methods

Tissue samples and tissue microarray (TMA)

Human FFPE tissue was used throughout this study. Both healthy and diseased samples were used for antibody and panel validation. Study samples included a tonsil section and four TMAs with sections arrayed in duplicate 1 mm

Table 1 Samples profiled by MIBI.

Sample type	Number of samples
Breast carcinoma	4
Colonic adenocarcinoma	4
Endometrial adenocarcinoma	3
Gastric adenocarcinoma	4
Head and neck squamous cell carcinoma	4
Lung adenocarcinoma	3
Lung squamous cell carcinoma	2
Melanoma	3
Non-Hodgkin lymphoma	3
Ovarian carcinoma	3
Prostatic adenocarcinoma	3
Renal cell carcinoma	3
Small cell lung carcinoma	2
Thyroid carcinoma	3
Tonsil	3
Urothelial carcinoma	3

Samples for MIBI were selected from TMAs with sections arrayed in duplicate 1 mm cores. Selection of cores was based on H&E staining to identify cores with both tumor and immune infiltrates present. Fields of view consisting of 500 μ m by 500 μ m were imaged for select cores with 1 FOV per core.

cores comprising bladder, breast, colon, endometrial, gastric, head and neck, lung, lymphoma, melanoma, ovarian, prostate, renal, and thyroid tumors (Table 1). Overall, 4- μ m-thick tissue was cut from blocks and adhered to MIBI slides (IONpath, Menlo Park, California); these conductive microscope slides are required by the MIBIScope to avoid issues that would otherwise arise from the charged ions of the primary ion source.

Antibodies and antibody conjugations

A summary of antibodies, their isotope labels, and the concentrations used for staining are listed in Table 2. Immunohistochemistry (IHC) was performed to select antibody clones on the basis of sensitivity and specificity using tissue microarrays composed of numerous different nonneoplastic and neoplastic tissue types, including unremarkable tissues known to be rich in immune cells with expected staining patterns, such as tonsil and thymus, and unremarkable tissues known to contain sparse immune infiltrates, such as placenta and liver. Specificity and sensitivity were determined using recommendations for IHC assays whenever possible [15]. For example, CD3 was shown to be moderately to strongly expressed on a predominance of cells within the interfollicular region of the tonsil as well as on scattered cells within the germinal center while expression was isolated to a few scattered immune

Table 2 Antibody panel used for staining tumor samples.

Target	Clone	Label	Cell expression	Localization	Conjugated antibody vendor and catalog number	Conjugated antibody titer (MIBI)
dsDNA	3519 DNA	89Y	All cells	Nuclear	IONpath, #708901	0.5 µg/mL
Beta-tubulin	D3U1W	166Er	All cells	Cytoplasmic	IONpath, #711301	1 µg/mL
HLA class I A, B, and C	EMR8-5	160Gd	All cells	Cytoplasmic	IONpath, #716001	1 µg/mL
Na-K ATPase alpha1	D4Y7E	176Yb	All cells	Cytoplasmic	IONpath, #717601	2 µg/mL
Keratin	AE1/AE3	165Ho	Tumor cells, epithelial cells	Cytoplasmic	IONpath, #716501	1 µg/mL
CD3	D7A6E	159Tb	T cells	Peripheral membrane	IONpath, #715901	1 µg/mL
CD4	EPR6855	143Nd	T helper cells, some macrophages	Peripheral membrane	IONpath, #714301	0.25 µg/mL
CD8	C8/144B	158Gd	Cytotoxic T cells	Peripheral membrane	IONpath, #715801	0.1 µg/mL
CD45	2B11 & PD7/26	175Lu	Immune cells	Peripheral membrane	IONpath, #717501	2 µg/mL
CD56	MRQ-42	150Nd	NK cells, neurons	Peripheral membrane	IONpath, #715101	0.05 µg/mL
CD68	D4B9C	156Gd	Macrophages	Peripheral membrane, cytoplasmic	IONpath, #715601	0.25 µg/mL
FOXP3	236 A/E7	146Nd	Regulatory T cells	Nuclear	IONpath, custom	4 µg/mL
PD-1	D4W2J	148Nd	T cells	Peripheral membrane	IONpath, #714801	0.5 µg/mL
PD-L1	E1L3N	149Sm	Tumor cells, macrophages, APCs	Peripheral membrane	IONpath, #714901	2 µg/mL
SOX10	BC34	170Er	Melanocytes, nerve cells	Nuclear	IONpath, custom	0.5 µg/mL

cells within the liver with no expression seen on hepatocytes. Antibodies with acceptable performance were then conjugated to elemental tags using MIBItag conjugation kits according to the manufacturer’s recommended protocol (IONpath). Labeled antibodies were tested by IHC and compared with the unconjugated antibody to verify that the conjugates had similar performance. The conjugated antibodies were titrated on serial TMA sections and MIBI staining was performed as detailed below. The optimal concentration was determined by analyzing the images and determining the concentration at which there was maximum signal in the cells of interest with minimal background. This was done qualitatively by visually assessing the images as well as quantitatively by analyzing the total ion counts obtained for a particular conjugated antibody in a single image. Numerous different tissue types were analyzed throughout the validation process to ensure the suggested lower limit of detection was achieved at the optimal concentration whenever possible [15]. An advantage of validating antibodies in a multiplexed assay is that expression of the marker in question can also be compared with the expression of others known to either show coexpression or a lack thereof. In this example, CD3 was seen to coexpress with either CD4 or CD8 and showed no coexpression with CD20, CD68, or pan-keratin, which helped provide further evidence that CD3 expression was isolated to T cells and was not expressed on B cells, macrophages or epithelial cells, respectively. In general, staining with metal-labeled antibodies uses a higher titer than what is used by IHC because MIBI staining does not have an amplification step. The antibody titer averaged 0.49 µg/mL for IHC (range 0.01–2 µg/mL) versus 1.08 µg/mL for MIBI (range 0.05–4 µg/mL). Figure S1 shows similar staining between IHC and MIBI for all antibodies used in the study.

MIBI staining

MIBI staining is performed similarly to traditional IHC. Slides were baked at 70 °C for 20 min, loaded onto a Histo-Tek SL Slide Stainer (Sakura, Torrance, CA), deparaffinized with xylene and then rehydrated through successive washes of ethanol (100% decreasing to 70%, Sigma-Aldrich, St. Louis, MO) and MIBI diH₂O (IONpath). The slides were transferred to a PT Module (Thermo Scientific, Waltham, MA) and heated to 97 °C for 40 min in epitope retrieval buffer (Target Retrieval Solution, pH 9, DAKO Agilent, Santa Clara, CA). The slides were blocked with 3% donkey serum (Sigma-Aldrich) in TBS-Tween (IONpath). The antibody panel was made by diluting antibody conjugates in blocking buffer and filtered using a centrifugal filter, 0.1 µm PVDF membrane (Ultrafree-MC, Merck Millipore, Tullagreen Carrigtowhill, Ireland). The slides were stained overnight at 4 °C in a humidity chamber.

Slides were loaded into the slide stainer and washed three times with TBS-Tween, fixed for 5 min in 2% glutaraldehyde (Electron Microscopy Sciences, Hatfield, PA), washed three times in 100 mM Tris pH 8.5 (IONpath), twice in MIBI diH₂O, and then dehydrated through a series of ethanol washes (70% increasing to 100%). The stained slides were stored in a vacuum cabinet for at least 1 h prior to loading into the MIBIScope.

MIBI acquisition

The MIBIScope is a dynamic secondary ion mass spectrometer (SIMS) instrument with a time of flight (ToF) mass analyzer [12, 13, 16]. The instrument used in this study had an Au (gold) liquid metal ion gun as the primary ion source, although other ion sources (O₂⁺, Xe⁺) are compatible with the instrument. Slides were placed onto a sample holder that was introduced into the system through a load lock chamber. The MIBIScope was focused primarily through adjustment of the primary ion gun's Lens2 voltage while imaging the tissue with the secondary electron detector (SED) that shows a live image of the topography of the tissue. Field of view (FOV) selection was performed via a point and click interface using a photo of the slide and confirmed with the live SED image. An H&E-stained section of each sample aided in FOV selection and the SED image available at the instrument during FOV selection was used to avoid tissue folds and areas of necrosis as much as possible. However, in cases where these regions could not be avoided, these regions were still imaged with the resulting data available for analysis, although regions of necrosis were not necessarily included in single cell analysis as these regions did not contain intact cells. FOVs that were 500 μm by 500 μm in size were selected at an imaging resolution of 1024 × 1024 pixels (~0.5 μm per pixel). Once the coordinates of all the FOVs were selected, the MIBI run was executed without any additional user input.

The MIBIScope rasters a primary ion beam across the tissue liberating secondary ions that are mass filtered to preferentially enrich for the isotopes introduced by the staining of the tissue with the metal-conjugated antibodies. An electrostatic analyzer within the MIBIScope acts as an energy filter, significantly biasing the ions detected towards monatomic species and reducing the transmission of polyatomics (hydrides, oxides, and organics). The mass of the secondary ions are determined using the orthogonal ToF mass spectrometer and the detected species were assigned to target biomolecules given the known isotopic label of each antibody creating 15-plex MIBItiff data files for all imaged FOVs. The data are reviewable using MIBItracker, an interactive, cloud-based data visualization tool (<https://mibi-share.ionpath.com>) in addition to being compatible with FIJI (ImageJ) and other tools through Bio-Formats.

Data analysis

An in-house pipeline for all data post processing was developed in Python 3.7, utilizing standard data analysis packages, such as numpy, skimage, and SimpleElastix. Mass calibration, inter-scan registration, and background and noise correction were performed using in-house developed algorithms (<https://github.com/ionpath/mibitracker-client>). Immediately after acquisition is completed, the raw data file is reduced by integrating all integral mass peaks (± 0.3 amu) into a TIFF file. Much of these functions have been automated through the MIBI/O software that is available as part of the MIBIScope platform. The resulting reduced TIFF image is significantly smaller than the raw data file, only about 5–10 MB per 1024 × 1024 FOV with 20 channels.

Cell segmentation takes advantage of the multiplexed nature of MIBI data by multiplying the nuclear dsDNA signal with the inverse of the sum of two membrane markers, Na-K-ATPase alpha1, and HLA class 1 A, B, and C, to accurately define boundaries in tissue images. First, four representative regions in terms of tissue structure and morphology, ~100 × 100 pixels in size, were annotated with cell centers. The cell centers were then used as seed points for watershed segmentation and served as ground truth data to determine optimal values for several watershed segmentation parameters, including a median filtering radius, sigma used to construct a gaussian kernel for additional smoothing, and minimum inter-cell distance. Values were determined using amoeba (Nelder-Mead) optimization. After optimal parameters were determined, an image was segmented using watershed segmentation. Boundaries were manually reviewed by visualizing nuclear, membrane, and cytoplasmic signals. As needed, cell segmentations were refined by adding, removing, or moving watershed seed points to ensure cell instances in a given image were accounted for. The result is an image in which each pixel is either assigned an integer value corresponding to a unique cell instance or 0, indicating a cell is not present. Figure S2 shows an example of the dsDNA nuclear marker with overlaid boundaries between cells.

Cell classification was performed with a custom pipeline written in Python 3.7 which builds up a set of hierarchical rules based on the markers present in the panel. In appropriate cases, rules were designed to be mutually exclusive such that cells containing markers with no expected co-expression could not be doubly positive, such as CD3 and CD68. Expression of markers were quantified at the single cell level using both a summed intensity and a cell score, which is a geometric weighted average of counts within a cell. Generally, the cell score was used for surface markers while the summed intensity was used for all others. Thresholds for each marker were determined by first

estimating based on the histogram distribution of score or intensity values throughout not just a single FOV but also across all FOVs. Refinement of the thresholds was done by visually comparing the cell classifications with the biological distributions seen in the images. Tumor boundaries were demarcated using keratin⁺ cells for the epithelial tumor samples and SOX10⁺ cells for the melanoma samples, where the boundary was smoothed using sequential morphological opening and closing operations.

Results

Antibody panel validation

In order to characterize a cohort of tumor samples for immune infiltrates, antibodies were selected specific to T cell subsets, macrophages, NK cells, vascular endothelial cells, and tumor cells in addition to the immuno-oncology targets PD-1 and PD-L1 (Table 2). IHC was first performed on the conjugated antibody to help determine staining accuracy by serving as the comparison method and ensuring the conjugation procedure did not significantly affect the affinity of the primary antibody (Fig. 1). IHC was performed using the same antigen retrieval conditions and antibody incubation time as noted in the methods for the MIBI staining. After determining the affinity of the

conjugated antibody had not been affected by the conjugation procedure, each conjugated antibody was analyzed on the MIBIScope at different concentrations on multiple different FFPE human tissue samples to determine the optimal concentration. Results were evaluated by comparing the MIBIScope expression pattern to the corresponding IHC, as well as visual comparison to markers expected to show expression on the same cell type or in the same compartment of the cell and markers not expected to show expression on the same cell type. Multiple conjugated antibodies can be tested simultaneously on the MIBIScope and the expression of these additional antibodies in relation to the antibody in question is often utilized to facilitate antibody validation.

An example of the antibody validation workflow for PD-L1 is shown in Fig. 2. PD-L1 (CD274) binds to PD-1 and inhibits T cell activation. Antigen presenting cells, activated T cells, and normal tissues including placenta, tonsil, and lung can express PD-L1. In disease, PD-L1 is expressed in cancer as a means for cancerous cells to inhibit immune responses [17]. PD-L1 has been detected within several tumor types including melanoma, lung, ovarian, colon, breast, and renal cell carcinomas. The PD-L1 E1L3N antibody clone (Cell Signaling Technology, Danvers, MA) was evaluated by IHC for specificity across normal tissue types. This clone was conjugated to the samarium isotope with a mass of 149 and IHC performed to verify comparable

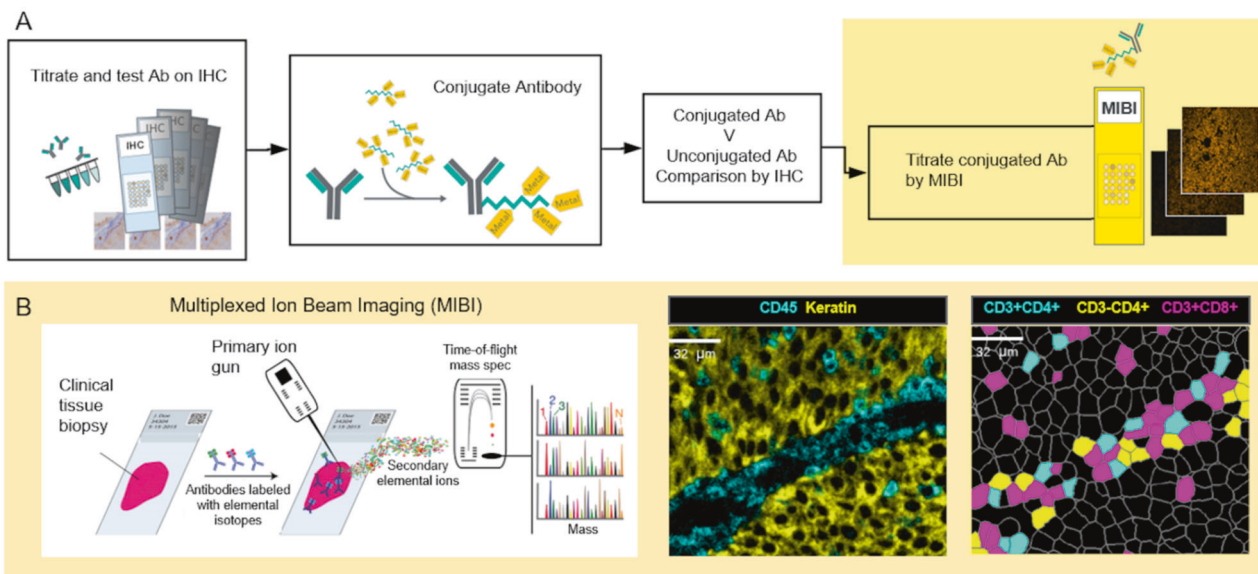


Fig. 1 Antibodies are rigorously tested and the resulting images produced by multiplexed ion beam imaging (MIBI) allow for segmented, phenotyped cells. **a** Illustration of antibody validation. Antibodies are tested by IHC using staining conditions consistent with the standard MIBI staining procedure. Clones that show the expected staining pattern in specific tissues are then advanced to the conjugation step where the antibody is isotopically labeled. The IHC performance of the labeled antibody is verified. Next, the labeled antibody is titrated using tissue microarrays and analyzed by MIBI to select the optimal

concentration of antibody. **b** Formalin-fixed paraffin-embedded (FFPE) samples are processed similarly to traditional IHC except staining is performed with a panel of isotopically labeled antibodies. An ion beam rasters across the tissue liberating ions including the isotopes bound to the tissue via the antibodies. Time-of-flight mass spectrometry separates the labels based on mass for detection of markers present across the tissue. Images can be segmented to define cell boundaries and marker combinations enable determination of cell phenotypes and distances between cells.

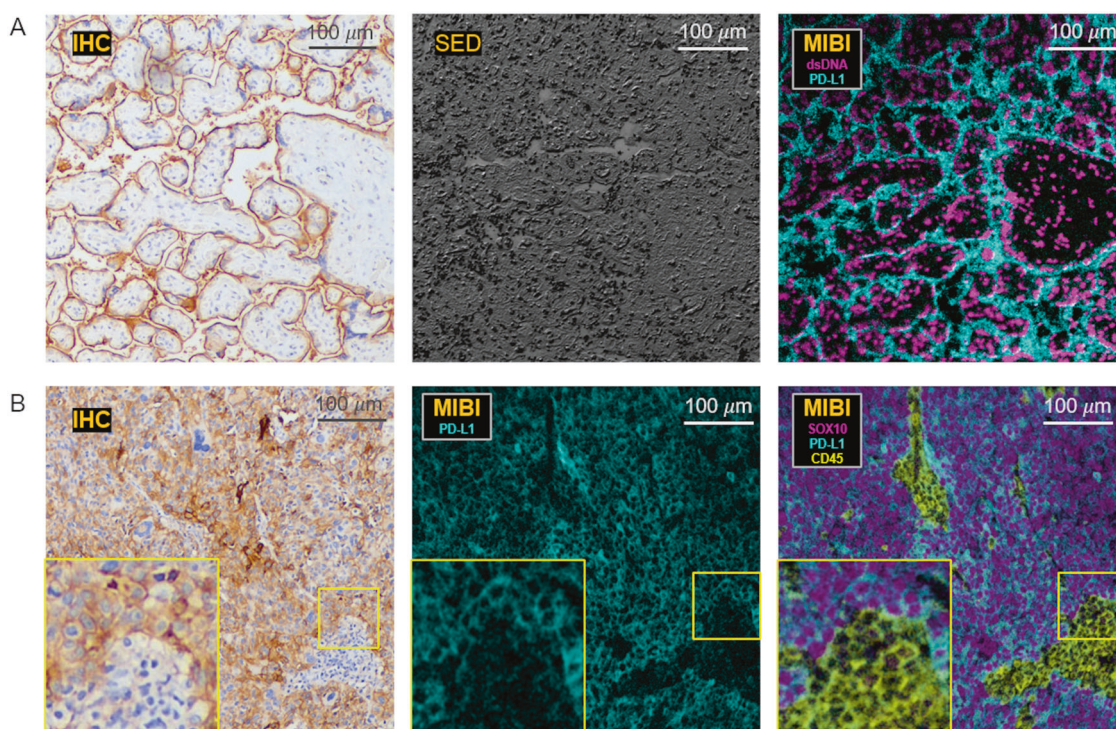


Fig. 2 PD-L1 antibody validation performed in healthy and diseased tissue using IHC and MIBI. **a** The top row shows PD-L1 staining of placenta. The IHC image is of a section cut ~10–20 slides away from the slide analyzed by MIBI. The secondary electron detector (SED) image corresponds to a 500- μm field of view (FOV) and was obtained by the MIBIScope at the time of FOV selection.

MIBI shows PD-L1_{149Sm} in cyan and dsDNA_{89Y} in magenta. **b** The bottom row shows PD-L1 in melanoma. The PD-L1_{149Sm} MIBIScope titration results are shown in cyan and SOX10_{170Er} (magenta) and CD45_{175Lu} (yellow) are overlaid illustrating the distribution seen with these markers in this melanoma sample.

staining performance with the unconjugated antibody. A similar staining pattern was observed for PD-L1_{149Sm} by MIBI as seen by IHC (Fig. 2a). Next, MIBIScope analysis was performed using a small panel that included an antibody to dsDNA. A tumor TMA was used to assess the staining performance of PD-L1 and other antibodies in the panel. PD-L1 was particularly prevalent in a melanoma sample as measured by IHC. When a section of the same melanoma sample was stained with metal-labeled antibodies including SOX10_{170Er} to identify tumor cells and CD45_{175Lu} to delineate immune cells, PD-L1 was observed to be widely distributed across SOX10-positive tumor cells (Fig. 2b).

After determining the optimal antibody concentration for each conjugated antibody by MIBIScope analysis, the next step was to assess the potential interference between antibody channels. The panel was built by taking into account the relative brightness of a target and the cell types the target is expressed on, the isotopic purity of the metal label (95–100%), and minimizing hydride, oxide and hydroxide spillover into neighboring target channels. An example of this is illustrated by the T cell markers in the panel. CD3, a pan-T cell marker, was placed on 159Tb, CD8 was conjugated to 158Gd, and 143Nd was used as the label for

CD4. Any signal from the hydride of CD8_{158Gd} and the oxide of CD4_{143Nd} would appear in the CD3_{159Tb} signal and importantly would not alter the interpretations gleaned from the data. Furthermore, isobaric impurities and other static mass interferences from hydrides, oxides and hydroxides can be computationally corrected using MIBI/O software (IONpath).

Leave-one-out (LOO) analysis was used to verify that the signal of an antibody channel was the result of the specific antibody and not influenced by another antibody conjugate [18]. Specifically, a single antibody is left out of the panel and the staining performance compared with tissue stained with the full panel. If there is an interference of one antibody (donor) into another (recipient) this will be apparent when the donor is absent in the LOO panel. A total of eight LOO panels were created and compared with the full panel. Staining of sections of a lung adenocarcinoma sample showed similar staining patterns across panels. Keratin_{165Ho} staining showed the same signal intensity and specificity toward tumor cells in panels lacking either PD-L1_{149Sm} or PD-1_{148Nd} as compared with the full panel (Fig. S3A). Conversely, tissue stained with a LOO panel lacking Keratin_{165Ho} showed negligible background and the oxide of PD-L1_{149Sm} was undetectable. Linear

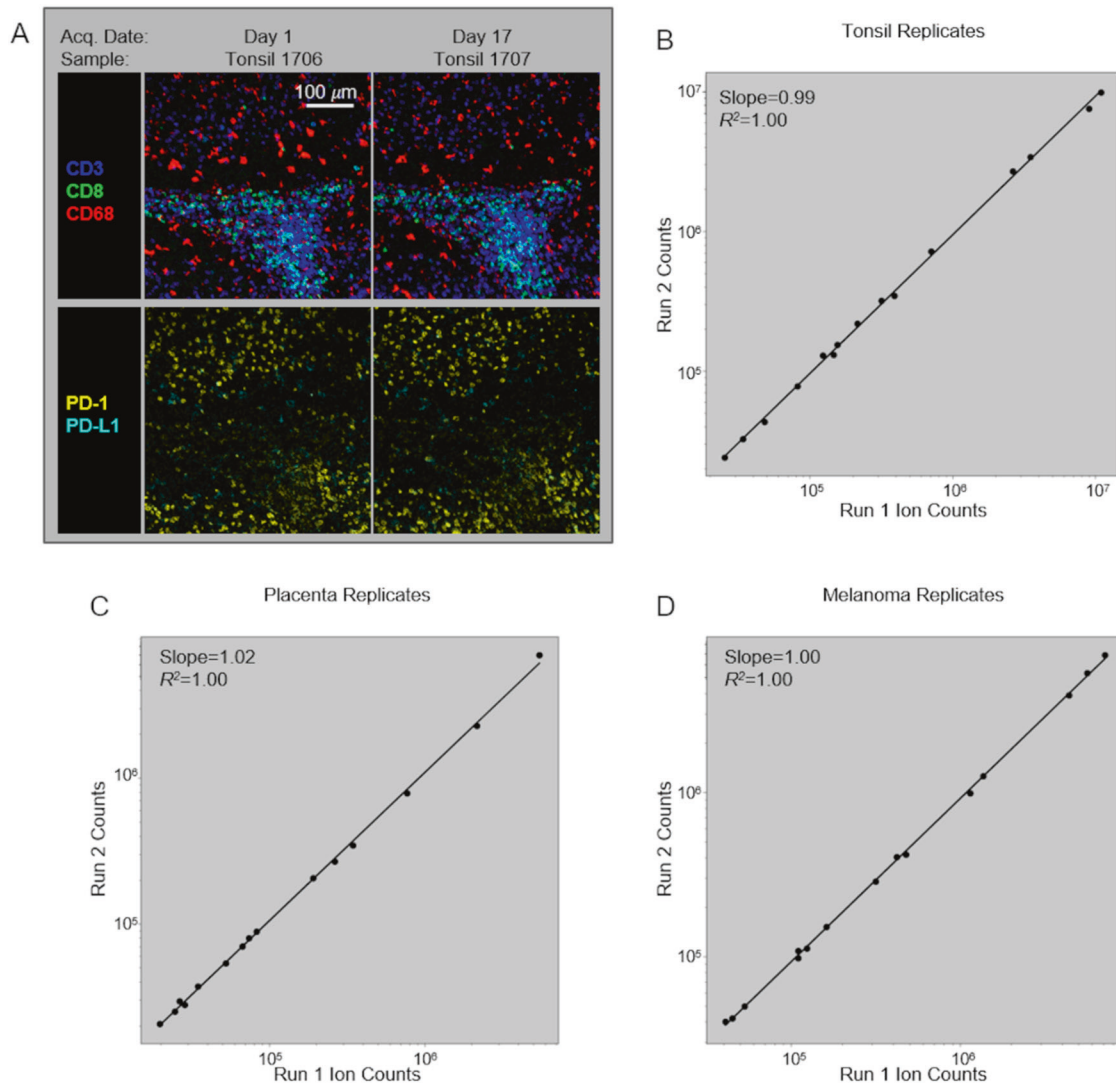


Fig. 3 Replicate samples acquired on the MIBIScope weeks apart show equivalent results. **a** Images of serial tonsil sections acquired by MIBI before and after acquisition of the sample cohort. **b–d**

Regression analysis comparing the signal of the 15 markers between the first replicate and the second replicate show repeatable results from MIBI acquisitions weeks apart.

regression of the signal of each marker as summed by the total ions collected within a FOW showed equivalent staining performance ($R^2 = 0.99–1.00$) between the full panel and panels lacking an antibody (Fig. S3B).

Cell type classification using MIBI of a diverse cohort of tumor samples

Following panel validation, the study slides were stained along with two control slides, with each control slide containing two serial TMA sections composed of either normal or neoplastic tissue samples. Comparison of the results acquired from the serial sections on the control slides (acquired at the beginning and end of the 2 ½ week study) showed similar staining performance. The matched FOVs show equivalent distributions of T cells and macrophages

with many of T cells also expressing PD-1 (Fig. 3a). Comparing the total ion counts for all of the markers between the two acquisition dates by linear regression showed excellent concordance ($R^2 = 1.00$, Fig. 3b–d). There was little, if any, signal drift during this time period as a result of instrument performance, making normalization of the data unnecessary (Fig. S4). These eight control images are available at <https://mibi-share.ionpath.com> in a user-friendly interface that enables visualization of the various markers in the panel with user-defined overlays. Furthermore, the detection of the metal tags uses SIMS, the most sensitive mass spectrometry technique for elemental analysis of surfaces [16, 19, 20].

A visual comparison of H&E images and MIBI FOVs shows similar tissue morphology between the sections of a number of tumor types (Fig. 4). Images acquired by MIBI

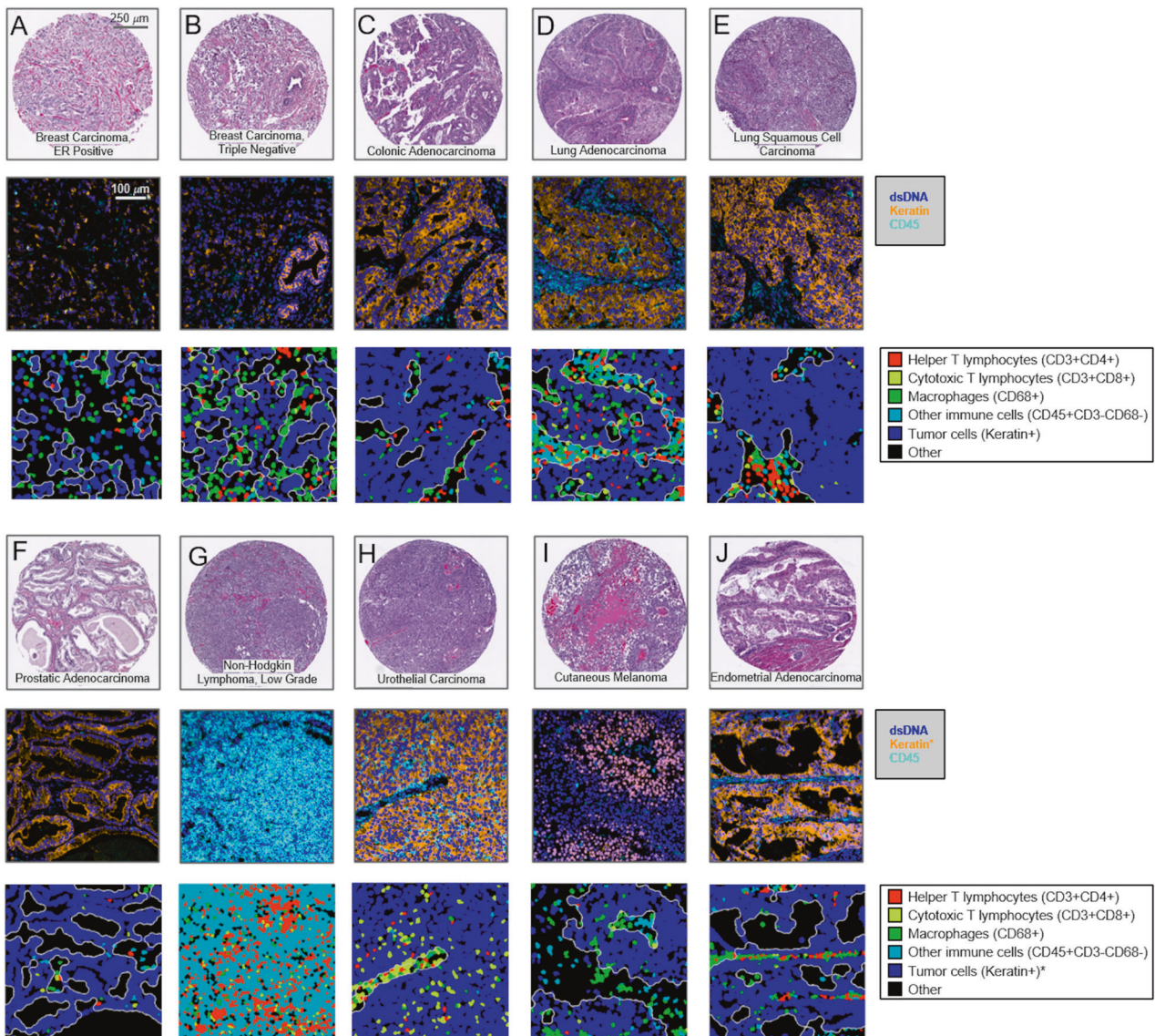


Fig. 4 MIBI produces complementary, deeper data to other imaging modalities across tumor types. Example images of ten tumor types comparing H&E images to MIBI. The MIBI images show a subset of the markers present in the panel and illustrate the spatial organization of keratin-positive tumor cells and CD45-positive immune cells within the epithelial tumor samples. The lymphoma

sample (g) does not express keratin, as expected. Segmentation was used to define cell boundaries and then the cells were classified to highlight the different immune cell subsets present within the samples. *Note that in the MIBI melanoma image SOX10 is used in place of keratin to identify tumor cells.

have morphological parameters, such as cellular size, density of cells, and spatial organization that are representative of the H&E images. Extending beyond this, MIBI analysis of CD45 and keratin or SOX10 expression reveals the spatial organization of immune and tumor cells within the various tumor samples. The tumor boundary was determined and then used to identify immune cells within the tumor and adjacent to the tumor. Some samples, like a triple negative breast carcinoma (Fig. 4b) and prostatic adenocarcinoma (Fig. 4f), showed an absence of immune cells within the FOV. Others such as a lung squamous cell carcinoma sample (Fig. 4e) or an endometrial adenocarcinoma sample

(Fig. 4j) had immune cells present but these were spatially enriched representing a compartmentalized TME. Other samples showed mixing of immune and cancer cells (lung adenocarcinoma, Fig. 4d; urothelial carcinoma, Fig. 4h).

Based on marker expression, cell instances from the segmented images can be classified into tumor and immune cell types using a decision tree. All of the samples were stained simultaneously with additional markers to further delineate the CD45⁺ immune subsets into CD68⁺ macrophages, CD3⁺CD4⁺ helper T cells, cytotoxic CD3⁺CD8⁺ T cells, and other immune cells defined as not T cells or macrophages. The samples showed varying frequency of

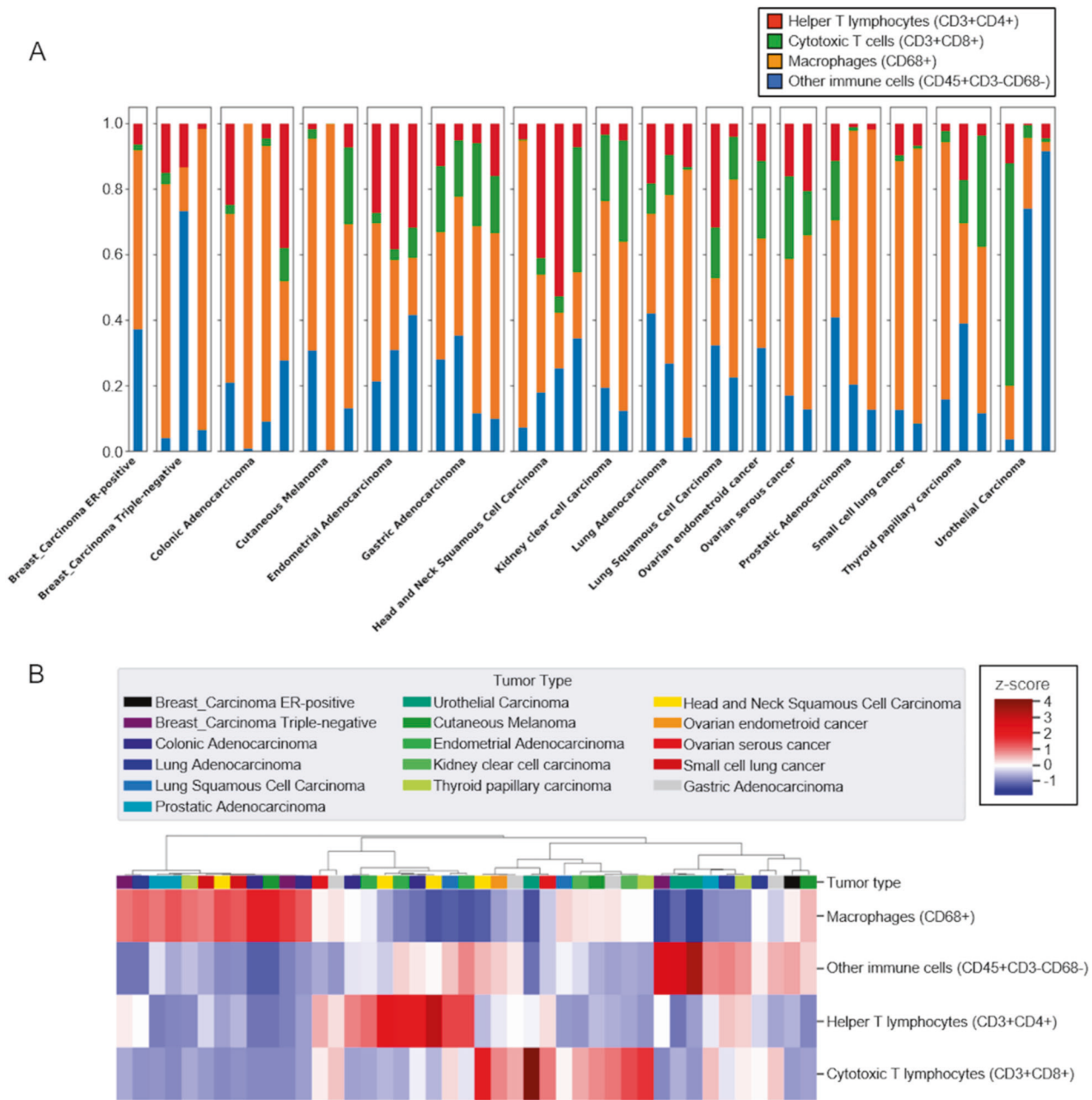


Fig. 5 Key cell types can be compared across tumor types. a Within the CD45+ cell fraction, the frequency of T cell subsets, macrophages and other immune cells are shown in the stacked bar chart. **b** Each

FOV and the frequency of the cell type are clustered using euclidean distances and the Ward metric (to minimize inter-cluster variance). Each cell type is normalized using its z-score (mean = 0 and std = 1).

these immune populations and did not appear to be associated with tumor type although this study was not powered to assess such associations (Fig. 5a). Nonetheless, there was an abundance of macrophages in most of the samples with a median frequency of 51% and range from 3 to 99% of the immune fraction whereas helper T cells (median frequency of 10% and range from 0 to 53% of the immune fraction) and cytotoxic T cells (median frequency of 5% and range from 0 to 68% of the immune fraction) were less abundant. Z-score normalization was performed using the population

frequencies and the resulting values were clustered identifying samples that shared similar population frequencies (Fig. 5b).

Spatial analysis of the TME

The distances between tumor-infiltrating immune cells and tumor cells have prognostic value in certain cancers. The spatial information available from MIBI can be used to quantify the distances between cells of different

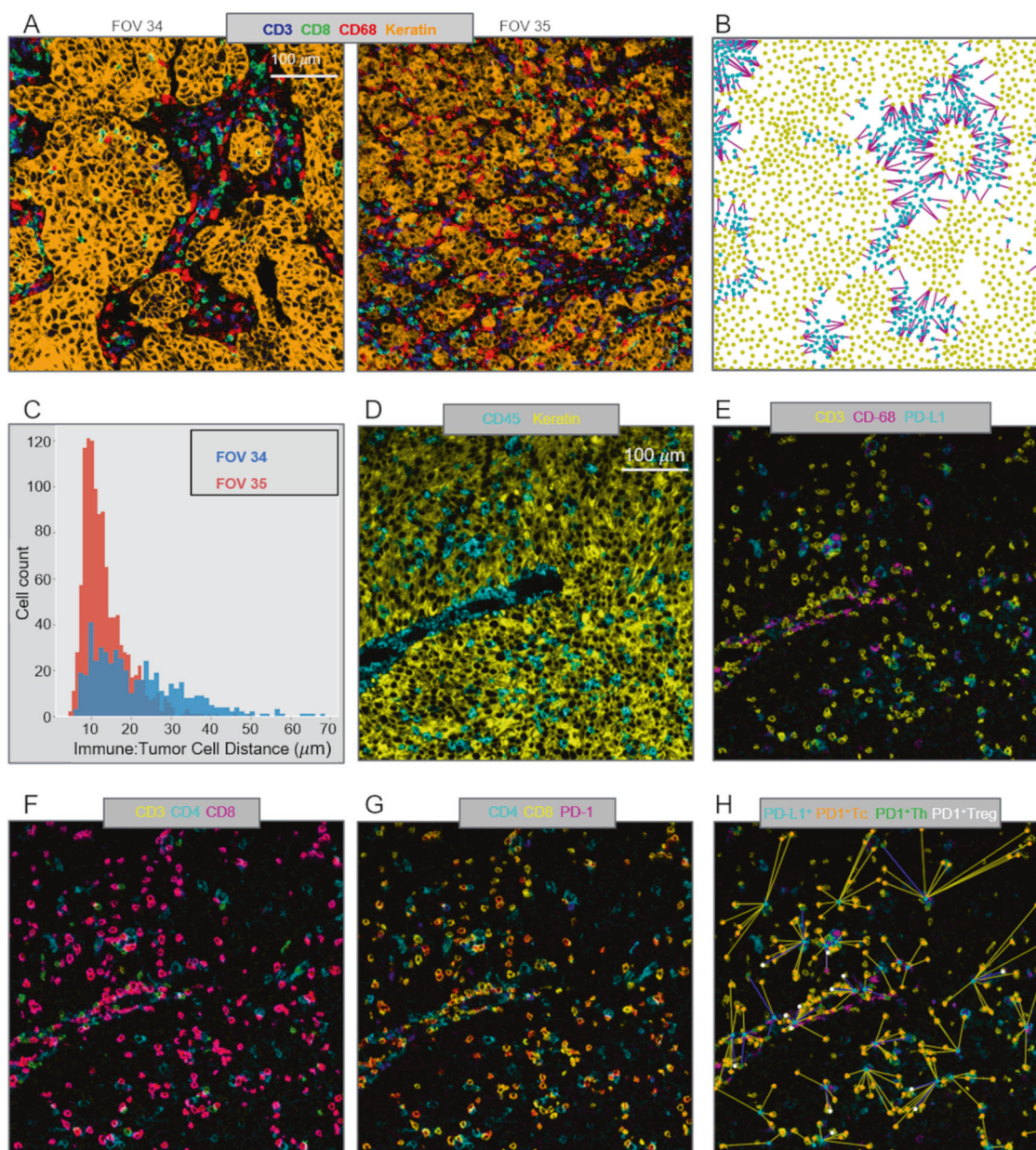


Fig. 6 Differences in the TME architecture: the spatial distribution of immune cells and tumor cells. **a** Ovarian serous carcinoma samples with CD3, CD8, CD68, and keratin overlaid show compartmentalized organization in FOV 34 and mixing of immune cells and tumor cells in FOV 35. **b** Pseudo coloring of cell populations highlighted in (A) with distances calculated between keratin⁺ cancer cells (yellow) and CD45⁺ immune cells (cyan). The spatial information provided by MIBI enables nearest-neighbor quantification of distances between tumor cells and the nearest immune cells. **c** The histogram of nearest-neighbor distances between tumor and CD45⁺ immune cells identifies

differences in TME architecture between FOV 34 and 35. **d** Urothelial carcinoma sample contains tumor cells and PD-1⁺ and PD-L1⁺ immune cells. Keratin⁺ tumor cells (yellow) and CD45⁺ tumor-infiltrating immune cells (cyan). **e** PD-L1 is detected on CD68⁺ macrophages (blue). **f** T helper cells (Th) are shown by CD3 and CD4 colocalization (green) and cytotoxic T cells (Tc) are identified by CD3 and CD8 colocalization (red). **g** PD-1 is expressed on a subset of Tc cells (red) and Th cells (blue). **h** The nearest neighbor distances between PD-L1⁺ cells and PD-1⁺ cells are calculated.

phenotypes. Two FOVs from different ovarian serous carcinoma samples showed similar amounts of infiltrating immune cells including CD8⁺ cytotoxic T cells and CD68⁺ macrophages (Figs. 5a and 6a). FOV 34 showed defined regions of tumor cells bordered by immune cells. In

contrast, FOV 35 showed immune cells scattered throughout the tumor. With the spatial coordinates of each cell mapped, the nearest neighbor distances for CD45⁺ immune cells and keratin⁺ tumor cells were calculated (Fig. 6b). FOV 34 had a greater distribution of cell distances as shown

by the overlay of histograms of the immune:tumor cell distances of FOV 34 and FOV 35 (Fig. 6c). Thus, even when the frequencies of cell populations are similar between samples, the organization of those populations to each other can vary dramatically, as revealed by MIBI.

Therapeutics targeting the PD-1/PD-L1 axis of immune regulation have shown clinical benefit in many patients. Understanding the mechanisms for response, or lack of one, is an area of active research. The presence of PD-1 and PD-L1 cells within the TME and their relative distances to one another has been reported to be a variable underlying clinical response [21]. To test if MIBI is suitable for measuring the distances between PD-1 and PD-L1 expressing cells, we performed spatial analysis on a urothelial carcinoma sample identified as having cells expressing these two markers. Immune cells were dispersed throughout the tumor sample (Fig. 6d) and PD-L1 was expressed on a subset of macrophages (Fig. 6e). CD3⁺CD8⁺ cytotoxic T cells were observed as the most abundant immune infiltrate (Fig. 6f). Many of these cytotoxic T cells expressed PD-1 as did some of the less-abundant T helper cells (Fig. 6g). Here again the nearest neighbor distances could be used to calculate the distance between PD-L1⁺ cells and PD-1⁺ cells (Fig. 6h).

Discussion

The ways in which a neoplastic cell arises and evades the immune system is the result of a departure from the systems biology that governs health. Understanding this biology requires methods that can resolve the heterogeneity of cell types, determine their states, whether they are activated (e.g., HLA-DR high) or suppressed (e.g., PD-1 high), and map their relationships or distances to one another. MIBI provides single cell resolution and sensitivity to phenotypically characterize the complex tissue environments including the TME. Executed similarly to IHC yet with the capability to profile 40+ markers simultaneously, MIBI is broadly applicable to a wide range of analyses performed in anatomic pathology including cell classification, spatial characterization, and assessment of marker expression. The MIBIScope produces data (multilayer TIFF files) that can be accessed by many analysis platforms currently available, such as those found in commercial software packages such as Fiji, Halo, and VisioPharm or freely available bioinformatic packages developed with open-source programming languages (e.g., R, Python).

All tumor types were stained, imaged, and analyzed using a single staining panel and standardized protocol. The workflow is flexible such that slides can be stained in batches and stored until imaged on the MIBIScope. Stained slides are typically stored under vacuum but protection from

light is not necessary as the labels are stable metal isotopes rather than light-sensitive fluorophores. Once imaged it is possible to reimagine the tissue as only a modest depth of the tissue is sputtered and analyzed during a single acquisition [16]. One limitation of the current project performed with an earlier version of the MIBIScope is the relatively small FOV size (500 μm by 500 μm) needed for images with 0.5 μm resolution. The current MIBIScope enables FOVs of 800 μm by 800 μm to be imaged in 70 min at fine resolution (650 nm). The resolution can be controlled at the instrument and acquisition at a slightly lower resolution than used in this study (1 μm) can be performed in 17 min. The 800 μm FOV captures 82% of a 1 mm TMA core. FOVs across cores of a TMA can be selected and then imaged in a single run. For whole sections it is possible to acquire adjacent images and stitch the images together using techniques commonly performed with other imaging technologies [22]. The need for tiling is particularly acute for imaging brain sections where multiple FOVs are collected to generate a larger image. Together with researchers at Stanford University, we are currently developing tiling methods to map large regions of brain tissue which will be described in a future publication. Because MIBI is still an early technology, the underlying methods for each stage of the processing pipeline are constantly evolving and improving, not just for accuracy but for generality. While the methods themselves are evolving, the pipeline tasks, at a high level, such as mass calibration, filtering, etc., are defined and have been automated through the MIBI/O software, and, as importantly, allows for appropriate user input when necessary. As more data becomes available, and the user base of MIBI grows, data processing should become more standardized.

The immediate utility of MIBI will be for understanding the biological mechanisms present in disease microenvironments. The results demonstrate the ability to detect a range of marker expression across many tumor types. The images can be segmented to define cell boundaries and then the expression of phenotypic markers used to classify cell instances into their cell class, such as proliferating tumor cells or nonproliferating tumor cells and various immune cells. Additional markers have been used on other sample sets to further define myeloid cell subsets, B cell subsets and stromal elements including vascular endothelial cells. This study also demonstrated the possibilities for calculating distances between different cell subsets including tumor and immune cells in addition to PD-1 and PD-L1 expressing immune cell subsets.

Although only a few clinical assays measure more than a few protein markers, there is clearly a strong need for more predictive assays. This is especially acute for immune checkpoint inhibitors that demonstrate efficacy of 20–30% in certain tumor types. Recently a companion diagnostic

assay for pembrolizumab has been developed based on IHC evaluation of PD-L1 expression in tumor biopsies. The overall response rate of 41% was achieved in patients with more than 50% of tumor cells positive for PD-L1 compared with an overall response rate of 20.6% in all patients in the study [23]. Clearly the presence of PD-L1 is a predictor of response but is not sufficient for accurately predicting response. A recent review of assays that predict response to anti-PD-1/PD-L1 showed that mIHC/IF had greater performance than PD-L1 IHC [24]. The hypothesis that additional biology underlies this response has appeal and has ultimately been waiting for tools that can measure the broader TME, particularly at the protein and cell level. As multiplex IHC technologies gain broader adoption it will be exciting to test if more sensitive and predictive assays can be developed to guide treatment.

A recent study using MIBI to analyze triple negative breast cancer samples showed a positive association between overall survival and the presence of compartmentalized histology, in which immune cells and tumor cells are spatially segregated, in contrast to samples that showed mixing of immune and tumor cells [12]. In a separate blinded study, MIBI was used to quantify the intensity of HER2 expression and percent of HER2-positive cells in breast carcinoma samples and the results strongly correlated with pathologist-derived HER2 IHC score [14]. In conclusion, MIBI provides a complementary tool to molecular genomics and digital imaging techniques being used to characterize the TME. Future studies using the subcellular resolution and multiparametric capabilities of MIBI should yield additional insights into the drivers of immune dysfunction within the TME.

Compliance with ethical standards

Conflict of interest JP, RF, MA, JT, YS, YZ, MN, and JF are employees of Ionpath Inc. DL, M-EC, and ZL are employees of Bristol-Myers Squibb.

Publisher's note Springer Nature remains neutral with regard to jurisdictional claims in published maps and institutional affiliations.

References

- Galon J, Costes A, Sanchez-Cabo F, Kirilovsky A, Mlecnik B, Lagorce-Pagès C, et al. Type, density, and location of immune cells within human colorectal tumors predict clinical outcome. *Science*. 2006;313:1960–4.
- Mlecnik B, Tosolini M, Kirilovsky A, Berger A, Bindea G, Meatchi T, et al. Histopathologic-based prognostic factors of colorectal cancers are associated with the state of the local immune reaction. *J Clin Oncol*. 2011;29:610–8.
- Galon J, Pagès F, Marincola FM, Angell HK, Thurin M, Lugli A, et al. Cancer classification using the Immunoscore: a worldwide task force. *J Transl Med*. 2012;10:205.
- Galon J, Fox BA, Bifulco CB, Masucci G, Rau T, Botti G, et al. Immunoscore and Immunoprofiling in cancer: an update from the melanoma and immunotherapy bridge 2015. *J Transl Med*. 2016;14:273.
- Tsujikawa T, Kumar S, Borkar RN, Azimi V, Thibault G, Chang YH, et al. Quantitative multiplex immunohistochemistry reveals myeloid-inflamed tumor-immune complexity associated with poor prognosis. *Cell Rep*. 2017;19:203–17.
- Philips GK, Atkins M. Therapeutic uses of anti-PD-1 and anti-PD-L1 antibodies. *Int Immunol*. 2015;27:39–46.
- Harnett MM. Laser scanning cytometry: understanding the immune system in situ. *Nat Rev Immunol*. 2007;7:897–904.
- Gorris MAJ, Halilovic A, Rabold K, van Duffelen A, Wickramasinghe IN, Verweij D, et al. Eight-color multiplex immunohistochemistry for simultaneous detection of multiple immune checkpoint molecules within the tumor microenvironment. *J Immunol*. 2018;200:347–54.
- Goltsev Y, Samusik N, Kennedy-Darling J, Bhate S, Hale M, Vazquez G, et al. Deep profiling of mouse splenic architecture with CODEX multiplexed imaging. *Cell*. 2018;174:968–e15.
- Nuñez J, Renslow R, Cliff JB 3rd, Anderton CR. NanoSIMS for biological applications: current practices and analyses. *Biointerphases*. 2017;13:03B301.
- Chang Q, Ornatsky OI, Siddiqui I, Loboda A, Baranov VI, Hedley DW. Imaging mass cytometry. *Cytometry A*. 2017;91:160–9.
- Keren L, Bosse M, Marquez D, Angoshtari R, Jain S, Varma S, et al. A structured tumor-immune microenvironment in triple negative breast cancer revealed by multiplexed ion beam imaging. *Cell*. 2018;174:1373–e19.
- Angelo M, Bendall SC, Finck R, Hale MB, Hitzman C, Borowsky AD, et al. Multiplexed ion beam imaging of human breast tumors. *Nat Med*. 2014;20:436–42.
- Rod S, Giltneane J, Bordeaux JM, Hitzman C, Koeppen H, Liu SD. Multiplexed ion beam imaging analysis for quantitation of protein expression in cancer tissue sections. *Lab Investig*. 2017;97:992–1003.
- Torlakovic EE, Nielsen S, Francis G, Garratt J, Gilks B, Goldsmith JD, et al. Standardization of positive controls in diagnostic immunohistochemistry. *Appl Immunohistochem Mol Morphol*. 2015;23:1–18.
- Keren L, Bosse M, Thompson S, Risom T, Vijayaragavan K, McCaffrey E, et al. MIBI-TOF: a multiplexed imaging platform relates cellular phenotypes and tissue structure. *Sci Adv*. 2019;5: eaax5851.
- Zou W, Wolchok JD, Chen L. PD-L1 (B7-H1) and PD-1 pathway blockade for cancer therapy: Mechanisms, response biomarkers, and combinations. *Sci Transl Med*. 2016;8:328rv4.
- Takahashi C, Au-Yeung A, Fuh F, Ramirez-Montagut T, Bolen C, Mathews W, et al. Mass cytometry panel optimization through the designed distribution of signal interference. *Cytometry A*. 2017;91:39–47.
- Hervig RL, Mazdab FK, Williams P, Guan Y, Huss GR, Leshin LA. Useful ion yields for Cameca IMS 3f and 6f SIMS: Limits on quantitative analysis. *Chem Geol*. 2006;227:83–99.
- Wilson RG. SIMS quantification in Si, GaAs, and diamond—an update. *Int J Mass Spectrom Ion Processes*. 1995;143:43–49.
- Giraldo NA, Nguyen P, Engle EL, Kaunitz GJ, Cottrell TR, Berry S, et al. Multidimensional, quantitative assessment of PD-1/PD-L1 expression in patients with Merkel cell carcinoma and association with response to pembrolizumab. *J Immunother Cancer*. 2018;6:99.
- Preibisch S, Saalfeld S, Tomancak P. Globally optimal stitching of tiled 3D microscopic image acquisitions. *Bioinformatics*. 2009;25:1463–5.

23. Hofman P, Badoual C, Henderson F, Berland L, Hamila M, Long-Mira E, et al. Multiplexed immunohistochemistry for molecular and immune profiling in lung cancer-just about ready for prime-time? *Cancers*. 2019;11:283.
24. Lu S, Stein JE, Rimm DL, Wang DW, Bell JM, Johnson DB, et al. Comparison of biomarker modalities for predicting response to PD-1/PD-L1 checkpoint blockade: a systematic review and meta-analysis. *JAMA Oncol*. 2019;5:1195–204.